Supporting Information

Effects of cerium oxide and ferrocene nanoparticles addition as fuel-borne catalysts on diesel engine particulate emissions: Environmental and health implications

Zhi-Hui Zhang, Rajasekhar Balasubramanian*

Department of Civil and Environmental Engineering, Faculty of Engineering, National University of Singapore, 1 Engineering Drive 2, E1A 02-19, Singapore 117576, Singapore

* Corresponding address: Tel.: +65 65165135; fax: +65 67744202

E-mail address: ceerbala@nus.edu.sg (R. Balasubramanian).

Experimental Section

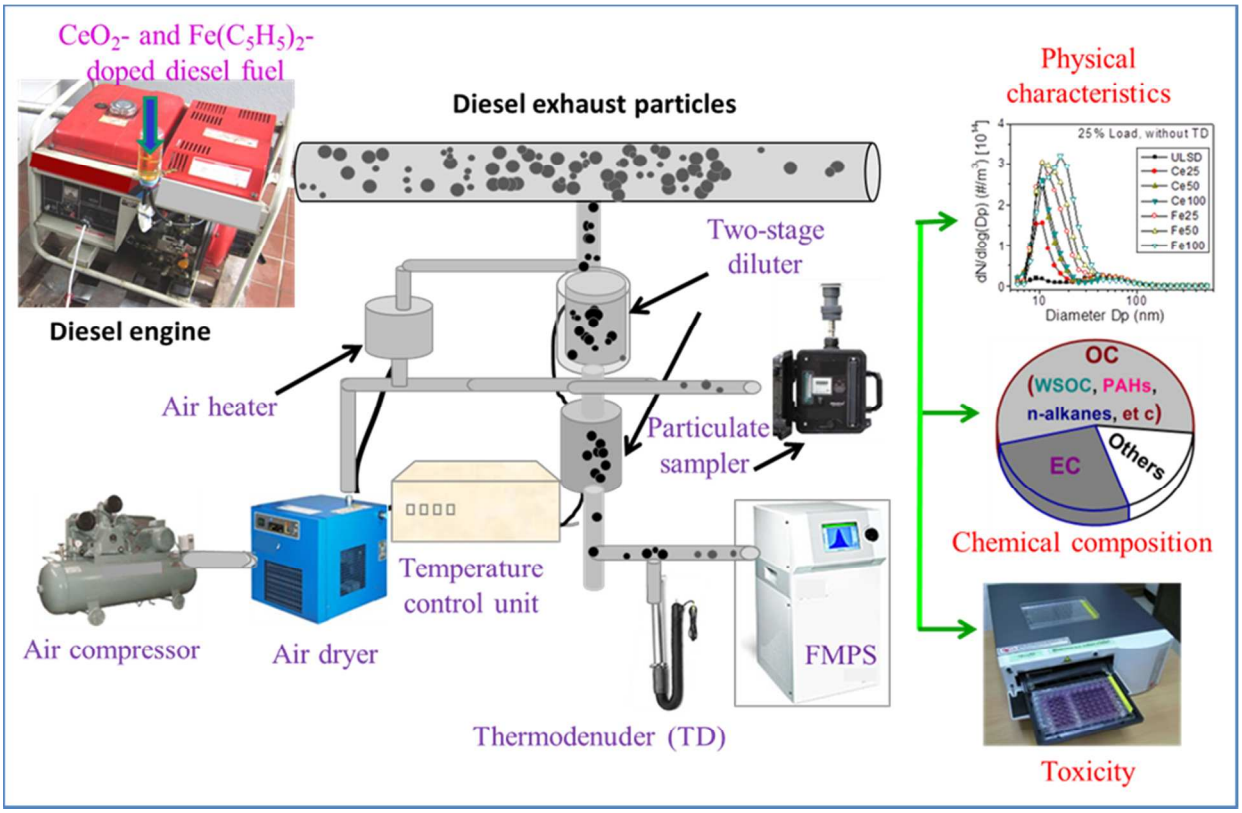

Figure S1 Schematic of the experimental system (FMPS-fast mobility particle sizer)

Table S1 Engine specifications

Model	Yanmar L70AE-DGY5B
Type	Single-cylinder, vertical 4-stroke, natural- aspirated, air-cooled diesel engine
Maximum power (kW)	4.5
Engine speed (rpm)	3000 rpm
Bore × stroke (mm)	78 × 62
Displacement (ml)	296
Compression ratio	20:1
Combustion system	Direct injection
Fuel injection timing (BTDC)	15
Injection pressure (bar)	196
Nozzle diameter × holes (mm)	0.24 × 4

The procedures of doping CeO_2 and $Fe(C_5H_5)_2$ to diesel fuel. Both CeO_2 and $Fe(C_5H_5)_2$ were added to the fuel as per the procedure reported by Sajith et al.,[1] and Miller et al.[2] and Nash et al.[3]. Briefly, the required quantity of FBCs was firstly measured using a microbalance (Sartorius MC5, an accuracy of ± 1 μg) for each experiment. The required quantity of CeO_2 for each does level was then mixed with ULSD by means of a water-bath sonicator (Elmasonic S 60H, ELMA, Germany), at a constant agitation time of 30 minutes to produce a uniform suspension. As for $Fe(C_5H_5)_2$, a known amount of $Fe(C_5H_5)_2$ was added to approximately 400 ml of ULSD in a glass beaker. This mixture was heated to 60 ℃, stirred continuously for at least 30 min, and further diluted with the appropriate mass of ULSD to achieve the desired Fe concentration. The modified fuels were utilized immediately after preparation, in order to avoid any settling of FBCs.

Determination of the dilution ratio and the handling of filters and DPM samples. A two-stage Dekati mini-diluter (DI-2000, Dekati Ltd.) was used for diluting the engine exhaust gas for DPM sampling and online evaluation. The diluter provides the primary dilution in the range of 8:1 to 6:1, depending on the engine load, while the secondary dilution system makes a further dilution of 8:1. The actual dilution ratio was determined based on the measurement of CO_2 concentrations in the raw exhaust, in the diluted exhaust and in the background air. The CO_2 concentration was measured with a non-dispersive infrared analyzer (Vario Plus, MRU, Germany; ± 0.5% accuracy). This measurement was done for every test, and all data presented in this article have been dilution-corrected to represent tailpipe conditions.

In this study, particles collected on the Teflon filters were used for gravimetric, water-soluble organic carbon (WSOC), and toxicological analysis, while those collected on quartz fiber filters were processed for subsequent OC/EC, thermogravimetric (TGA) and Raman spectra

analysis. Unfortunately, blank quartz fiber filters usually contain microgram-level of organic carbon per cm^2 of the filter, which is higher than the lower detection limit for OC/EC and some specific organic compounds. This potential interference could therefore affect the final results. In order to avoid this interference from blank filters, the blank quartz fiber filters were pre-combusted in air (650 ℃ for 12 h) in a muffle furnace to remove any residual carbon contamination prior to being used for particles collection. This approach is widely used for removing the organic compounds in the blank quartz filters. Before and after sampling, the filter samples were conditioned in a humidity-controlled chamber (22 ± 3 ℃ and 30 ± 8% RH), and weighed using a microbalance (Sartorius MC5, accuracy of ± 1 μg) to determine the collected particulate mass. After being weighed, the filter samples were kept in glass petri dishes and stored under refrigeration at -20 ℃ until extractions and analyses to minimize loss of semi-volatile organic compounds. Meanwhile, the glass dishes were wrapped in aluminum foils to prevent light penetration, potential light-induced chemical reactions and contamination. The dishes were further wrapped in a waterproofing membrane.

Physical analyses. A thermogravimetric analyzer (Discovery TGA, TA instruments) was used to investigate oxidation properties of soot followed by the method reported previously.[4] Briefly, the particle samples were firstly heated in the argon environment to remove the volatile organic fraction (VOF). The remaining part (soot) was continually heated at an air environment to investigate soot oxidation reactivity. The ignition temperature was determined as the temperature at which the rate of mass loss at the air environment reaches the maximum. The activation energy for the soot was then estimated using a modified form of the Arrhenius expression, as suggested in Stratakis and Stamatelos.[5]

Raman spectra of the DPM samples were recorded with a Renishaw microscope system (Renishaw, System 2000) using a 514 nm Ar ion laser as an excitation source. The Raman spectral intensity and wavelength were calibrated with the silicon wafer by utilizing the first-order Stokes Raman of pure Si at 520 cm^{-1}. The spectra of the DPM samples were in the range of 100 – 3600 cm^{-1} with a 50X magnification objective and with a spectral resolution of ~3.5 cm^{-1}. The Raman spectrometer was generally operated in the continuous scanning mode. The power of the excitation laser beam (1–100% relative intensity), spot diameter (0–100% defocusing), and exposure time were varied to find optimum measurement conditions. For each sample, ten spectra collected at different positions were analyzed and averaged in each sample in order to improve the statistical significance. The Renishaw WIRE 2.0 software running under GRAMS/32 (Galactic, Levenberg–Marquardt nonlinear least-squares fitting algorithm) was used to perform the spectral analysis. The spectral parameters of the soot were determined by the curve fitting after linear baseline correction. To ensure the reproducibility of the curve fit, the fitting procedure was repeated at least five times for each Raman spectrum.

Toxicological experiments. We followed the same experimental protocol for the extraction of particles from filters for toxicity study as the validated procedures reported in the literature.[6] Briefly, the particulate samples were firstly extracted from the Teflon filters by using methanol in the water-bath sonicator (Elmasonic S 60H, ELMA, Germany) for 2 × 30 min, subsequently concentrated in a rotary evaporator (Buchi, Switzerland) to 5 ml, and then dried under ultrapure nitrogen flow (100 ml/min), and finally stored at -20 ℃. The extraction efficiencies were in the range of 88-95%, and the extracted particulate mass was efficiency-corrected. The extracts were re-suspended in DMSO (Dimethyl sulfoxide, Bioreagents, Sigma-Aldrich) and subsequently in cell exposure medium. We exposed the particles to the human-type

II cell alveolar epithelial cell line (A549). The cytotoxicity of these particles was measured by using the MTT assay and the resulting changes in the expression of global genes were carefully assessed by using the cDNA microarray technique.

For MTT assay, the A549 cells were cultured in DMEM (Dulbecco's Modified Eagle Medium, Gibco) with 10% FBS (fetal bovine serum) at 37 ℃ in 5% CO_2. A549 cells were seeded into 96-well plates at a concentration of 1×10^5 cells/ml, and cultured for 24 h to allow adherence and proliferation. The medium was then replaced, and the cells were exposed to particles contained DMEM and control for another 24 h. The final concentrations of particles in the cell culture wells corresponded to 25, 50, 100 and 200 μg/ml of native particles. The final concentration of DMSO in the medium did not exceed 0.5% (v/v). At the end of the treatments, MTT (3-(4,5-Dimethylthiazol-2-yl)-2,5-diphenyltetrazolium bromide, a yellow tetrazole, Sigma-Aldrich) (0.5 mg/ml final concentration) was added to the wells and incubated for 4 h. The medium was removed, and 100 μl DMSO was added to each well for dissolving the blue formazan crystals. The absorbance value of the MTT formazan in each well was measured using an Infinite 200 PRO microplate reader (Tecan Group Ltd, Germany) at a wavelength of 570 nm. Each sample was tested in six replicate wells, and the data on cell viability are reported as a relative decrease compared to the control, considered as 100% of viable cells.

As for gene expression, A549 cells were exposed to 50 μg/ml of particles or 0.1% DMSO (control) for 6 hours. This concentration and exposure duration are the suitable conditions for evaluating the acute influence of DPM in the low level of cytotoxicity as suggested by Koike et al.[7] After exposure, total RNA was extracted using RNeasy Mini Kit (Qiagen Cat. No. 74104). The RNA concentration was measured with Nanodrop (ND-1000, NanoDrop Technologies Inc., Wilmington, DE) and the RNA integrity was assessed using the RNA 6000 Nano Chip kit

(Bioanalyzer 2100, Agilent technologies, Amstelveen, The Netherlands). The RNA samples with RNA Integrity Number (RIN) > 7 was used for reverse transcription. 500 ng of total RNA was used for reverse transcription with T7 Oligo(dT) primer using SuperscriptTM II Reverse Transcriptase (Invitrogen). This step will allow us to synthesize the first-strand cDNA with T7 promoter. The single-strand cDNA was further converted into the double-strand DNA (dsDNA) template for transcription. In vitro transcription for cRNA synthesis was conducted in a biotinylated cRNA amplication step with Illumina Total Prep RNA Amplification Kit. 750 ng of cRNA was hybridized to HumanHT-12 v4 Expression BeadChip Kit (Illumina) according to the manufacturer's instructions. The bound cRNA was visualized by binding streptavidin-Cy3 (GE healthcare) conjugates to the BeadChip, followed by scanning the arrays using Illumina Bead Array Reader. The signal values of cRNA bound to each probe were further translated into gene expression values using Partek® Genomics Suite™ version 6.5 (Partek Inc., USA).

The microarray signals were quantified with Partek Genomic Suite version 6.4 (Partek) and the intensities were normalized using the robust multiarray analyses background correction (RMA). Principal component analysis (PCA) was performed before analysis of gene expression to ensure quality control. Analysis of variance (ANOVA) was conducted on the complete data set and a list of differentially expressed genes was obtained using FDR (False Discovery Rate, Benjamini Hochberg post hoc) of 0.05 with a 1.5-fold cut-off for fold-change. To discover enriched functional-related gene groups in our study, the genes shortlisted from microarray data was conducted with Gene Ontology (GO) analysis. The identified gene list has undergone functional annotation clustering using the DAVID web resource (http://david.abcc.ncifcrf.gov/). The tested categories are Biological Processes and KEGG.

Quality assurance and control (QA/QC). At each mode of operation, the diesel engine was allowed to run at least for half an hour to ensure the primary fuel remaining in fuel lines and fuel pump was completely consumed. The engine running parameters such as the exhaust gas temperature and the power output, attained steady-state values and data were measured subsequently. For particulate mass concentration determination, three independent measurements were carried out for each operating condition with particulate samples collected in duplicates for each measurement. For determining particle number concentrations and size distributions, five measurements were taken at each independent measurement of each mode of operation and the corresponding mean values were calculated.

For the OC/EC analysis, the particulate mass collected on each quartz fiber filter was within the best detection range of 5 to 400 $\mu g/cm^2$ for OC and 1 to 15 $\mu g/cm^2$ for EC. The collected particulate mass was sufficient for repeated analysis of EC and OC to confirm the reproducibility of data. Duplicate analyses on the same sample were done for each five samples to verify the precision of the Sunset Laboratory method of OC/EC analysis. In this study, the overall relative standard deviation (RSD) of these replicates was estimated, which included any variation in sampling procedure, the sample density on the surface of the filter, and any instrumental variation. The accuracy of this method was routinely checks by analyzing a known quantity of sucrose and/or other organic compounds that were applied to blank quartz fiber filters. The lower detection limit of this method is on the order of 0.2 $\mu g/cm^2$ filter for both OC and EC, which can be translated into corresponding airborne concentrations. In order to take advantage of the low detection limits of this method, the quartz filters were pre-combusted to remove any residual carbon contamination. This is because blank quartz fiber filters which have not been

fired usually contain 2 to 5 μg of OC per cm^2 filter. Six blank filters were also analyzed and the sample results were corrected for the average of the blank concentrations.

Before WSOC analysis, the reagent grade Potassium hydrogen biphthalate ($C_8H_5KO_4$) was previously dried (110°C for about 1 hour), and then was dissolved into the organic-free Milli-Q water (>18 MΩ cm), and finally was diluted as standard solutions with different concentrations for calibration and recovery tests. A five-point calibration was performed, and the correlation coefficients (R^2) obtained from the linear regression of the calibration curves was larger than 0.99. Prior to the calibration, five repeated analyses of purified water containing 2-3 drops of HCl per 100 mL of solution were conducted by using the same procedure as used for the sample. Six standard samples were prepared by spiking a known amount of the standard solution to several pieces of pre-combusted blank quartz fiber filters, followed by a 5 min air drying. Subsequently, the standard samples were extracted, filtered, acidified, purged with ultrapure air, and finally were analyzed by TOC analyzer following the same protocol and using the same analytical parameters (injection volume, sparge time) as used for the diesel particulate matter samples. Based on the results, the recoveries were calculated after correction for the blank contribution. In the study, six blank filters were also analyzed. The lower limit of detection (LOD) of the methods was calculated as 3 times of the average value as the standard deviation of the six measurements of blank filter water extracts divided by the slope of the calibration curve. For each sample, four replicate analyses were done; the RSD of these replicates, including aliquot cutting, extraction procedure and instrument variability was estimated. For minimizing cross contamination during the analysis of filter samples, Milli-Q water was run prior to and after the calibration and randomly selected standards that were processed in between the analysis of the DPM samples. In addition, all the glassware used for experiments was firstly cleaned by

soaking in 5% HCl for 48 hours, and then was heated in air (500 ℃ for 4 h) in a muffle furnace to remove any residual carbon contamination, and finally were washed by Milli-Q water.

The details of QA/QC procedures for particle-phase PAHs and n-alkanes analyses are provided by Ho and Yu.[8] Briefly, calibration standards were prepared by spiking known amounts of PAHs and n-alkanes in liquid standard mixtures (Sigma-Aldrich, Bellefonte, PA, USA) and two deuterated compounds, n-tetracosane-d50 (n-C24D50) (98 %, Aldrich, Milwaukee, WI, USA) and phenanthrened10 (phed10) (98 %, Aldrich) as internal standards (IS) onto several small pieces of per-combusted blank quartz filters. The standard-loaded filters were then placed into the TD tubes for GC-MS analysis. Calibration curves were constructed by plotting the peak area ratios between the analytes and the respective IS (i.e., n-C24D50 for alkanes and phe-d10 for PAHs) versus the amounts of the analytes. In this study, an eight-point calibration over a concentration range of 0.1– 5.0 ng for each PAH and n-alkane was established, and the R^2 for linear regressions of the calibration curves was greater than 0.99. National Institute of Standards and Technology (NIST) Standard Reference Material (SRM) 1650b was employed to validate the accuracy of PAHs analyses. The relative error between the certified values in SRM 1650b and the calibration standard concentrations was <9.5%. The LOD of the method is defined as the minimum amount of an n-alkane or a PAH that generates the minimum distinguishable signal plus three times the standard deviation of the blank signals. No peaks were detected for either n-alkanes or PAHs in the blank calibration samples. As a result, we approximated the mean blank signal with the calibration line intercept and the blank signal standard deviation with the standard error for the y (peak area ratio) estimate, based on which the LODs were calculated. For each sample, four replicate analyses were done; the RSDs were then estimated. Six blank filters were

also analyzed, and all data were corrected for the average value of the blanks, and are reported as the mean values.

Results and Discussion

Discussion regarding the DPM formation processes. A fundamental understanding of the formation of new particles and their growth in diesel engines may explain how FBCs-doped fuels affect the DPM emissions. Diesel soot (EC) is formed during combustion by a series of processes that include nucleation, surface growth, coalescence, agglomeration and oxidation.[9] Nucleation refers to the formation of soot nuclei from the building blocks of aromatic compounds that originate from the soot precursors through fuel pyrolysis in the fuel-rich regions. These nucleated soot particles grow by attachment of gas-phase species to their surface, followed by a combination of two roughly spherically shaped particles to form a single spherically shaped particle through coalescence. These particles finally agglomerate to form long chain-like structures. Such agglomerated particles encounter the diffusion flame and are mostly oxidized at temperatures around 2500 K, but it is thought that some of these particles survive due to localized quenching and remain in the combustion chamber.[10] As the piston moves downward, the system cools rapidly. At this stage, if there are other non-volatile gaseous species (such as metals) with very high concentrations, they will deposit on the soot particles or may alternatively self-nucleate if the rapid cooling drives their saturation ratios high enough.[10] As the resulting soot particles subsequently travel through the exhaust system and dilution systems, further cooling causes their growth in size through condensation of semi-volatile and volatile species and/or self-nucleation of the latter into nanoparticles. These volatile and semi-volatile species originate from unburned fuels, lubricating oil, and combustion byproducts which escape oxidation and consist mainly of OC.[11] With the addition of FBCs to diesel fuel, the FBCs are

involved in the entire process of the combustion of vaporized liquid fuel, soot inception and oxidation, and final formation of DPM in the exhaust and dilution systems. Therefore, the factors that affect the formation and oxidation processes of soot in the combustion chamber of diesel engines determine the EC emissions, while the concentrations of organic compounds and the states of the cooling and dilution processes affect both the OC emission concentrations and the relative amounts of volatile substances that adsorb or condense onto pre-existing soot particles, or nucleate to form new particles.

The explanations regarding the formation and the evolutionary processes of metallic nanoparticles, and their influence of particle size distributions in response to changes in the proportion of FBCs used in ULSD and the engine load. During the early stage of engine combustion, the organic component of ferrocene decomposes due to its lower melting point, [12] and is most dominantly present in the form of amorphous Fe (III) oxide crystallizing to hematite α-Fe_2O_3.[13] This process was suggested to occur before the onset of soot particle inception,[14] and therefore homogeneously nucleated iron oxide nuclei and nanoparticles are subsequently created, leading to coagulation of these particles with each other and with other particles. Then, these self-nucleated particles, or their agglomerates would attach themselves directly to carbon surfaces, or undergo further coagulation with carbon particles. Therefore, with an increase in the level of iron doping, vapor deposition may not keep up with the locally high cooling rate and the supersaturation ratio of iron rises quickly, leading to the formation of more counts and larger sized metallic nanoparticles. Subsequently, as the soot is oxidized, the Fe occlusions present in the same soot particles may coalesce. If a soot particle is completely oxidized, the Fe particles are liberated, and continue to undergo particle-to-particle interactions and agglomeration.[3] Based on the results of our study, it is possible that the presence of the large counts of soot particles in

the accumulation mode associated with higher engine loads provided a large surface area for adsorption of these self-nucleated metallic particles, or their agglomerates that comprised the nucleation mode. This interaction enhances Fe coalescence and agglomeration during the soot oxidation process, resulting in a relatively lower increase in nucleation-mode metallic particles than that at lower engine loads. Compared to $Fe(C_5H_5)_2$, CeO_2 is also involved in the evolutionary processes including coalescence and agglomeration with each other and with other particles, and condensation /adsorption onto the surfaces of the agglomerates. Therefore, both Fe- and Ce-doped fuels share a similar trend with variations of particle size distributions in response to changes in the proportion of FBCs used in ULSD and the engine load. However, the nano-sized cerium oxide mixed with fuel should not be decomposed during diesel combustion due to its very high melting point (2200–2400 ℃) (i.e. very low vapor pressure). This is evident from the previous study by Jung et al.[15] who found that the metallic nanoparticles decorate the exterior of soot agglomerates. The higher melting point of cerium oxide may result in less favorable formation of self-nucleated metallic nanoparticles and therefore have a lower chance to further coagulate to bigger particles compared to Fe-doped fuels. This is evident from the lower peak of nucleation mode particles and a shift toward a smaller size compared to Fe-doped fuels as found in this study (see Figure 3). Meanwhile, the catalysts with high melting point would have low activity in soot combustion due to their low mobility, which in turn leads to higher emissions of soot from Ce-doped fuels than from Fe-doped fuels. The higher soot emission may provide more surface area for adsorption of these self-nucleated particles, or their agglomerates that comprised the nucleation mode and therefore led to a lower increase in nucleation-mode Ce-containing particles than that of Fe-doped fuels. In addition, under the same mass of FBCs, the Ce-based FBC may produce a lower number of metal atoms and thus a lower amount of their

nanoclusters. The difference in the number of metal atoms in the fuel, produced from their corresponding FBCs, is likely to contribute to the difference in the physico-chemical and toxicological properties of DPM observed in the study.

The overall effects of the FBCs-doped fuels on particle formation can be indicated by the metal/C ratios as suggested Miller et al.,[2] who concluded that the higher Fe/C ratio resulted in lower soot mass emissions, but a higher amount of Fe-riched nanoparticles. In this study, we further analyzed the relationship between mass flow of metals (Ce and Fe) and metal/C ratios, and between metal/C ratios and the counts of metallic nanoparticles, respectively, with the results shown in Figure S2. We found that the higher concentrations of Ce or Fe in diesel fuel resulted in the higher Ce/C or Fe/C ratios and higher counts of metallic nanoparticles. For the same dose of Ce or Fe doped to diesel fuel, the higher engine load resulted in the lower Ce/C or Fe/C ratios and thus a lower count of metallic nanoparticles. Therefore, it is likely that the lower carbon generation at lower engine load preferentially facilitates formation of self-nucleated metallic particles rather than their adsorption onto soot particles. With an increase of the level of doping FBCs, the increase in Ce and Fe combined with soot emission reduction due to the enhanced oxidation yields higher Ce/C and Fe/C ratios, leading to the elf-nucleated metallic particles nanoparticles having an increase in their counts and also in their size. In this study, we also found that for each tested condition, the Fe/C ratio was slightly higher than that of Ce/C ratio and therefore resulted in higher nanoparticles. These explanations are consistent with the discussion in the previous paragraph, and therefore further confirmed our hypothesis about the role of FBCs in soot particle formation and particle number emissions.

In order to analyze the variation of particle number concentrations in detail, the volatile particles were further classified into four groups: < 20 nm, < 50 nm, > 50 nm, and total particles (particles with diameter of 5.6-560 nm), which are shown together with the particle geometric mean diameter (GMD) in Table S2.

Table S2 Effect of FBCs-doped fuels on the number concentrations of size-segregated volatile particles and geometric mean diameter (GMD)

	ULSD	Ce25	Fe25	Ce50	Fe50	Ce100	Fe100
25% load							
$D_P < 20$ nm #/m^3 [10^{14}]	1.04 ± 0.05	6.27 ± 0.35	10.10 ± 0.61	10.90 ± 0.65	14.90 ± 0.97	16.70 ± 1.12	16.70 ± 1.17
$D_P < 50$ nm #/m^3 [10^{14}]	2.15 ± 0.09	7.13 ± 0.31	10.98 ± 0.53	11.72 ± 0.56	17.09 ± 0.89	19.94 ± 1.10	21.16 ± 1.24
$D_P > 50$ nm #/m^3 [10^{14}]	0.99 ± 0.04	0.94 ± 0.03	0.88 ± 0.03	0.73 ± 0.03	0.86 ± 0.04	0.81 ± 0.04	0.66 ± 0.04
D_P = 5.6-560 nm #/m^3 [10^{14}]	3.14 ± 0.13	8.07 ± 0.35	11.85 ± 0.56	12.46 ± 0.59	17.95 ± 0.93	20.75 ± 1.15	22.82 ± 1.28
DGM (nm)	29.00 ± 2.30	14.61 ± 2.04	15.12 ± 1.73	13.90 ± 1.85	15.70 ± 1.68	13.30 ± 1.73	16.71 ± 1.58
50% load							
$D_P < 20$ nm #/m^3 [10^{14}]	0.35 ± 0.02	0.45 ± 0.03	1.53 ± 0.09	5.34 ± 0.32	3.93 ± 0.26	9.24 ± 0.65	13.70 ± 0.96
$D_P < 50$ nm #/m^3 [10^{14}]	2.14 ± 0.08	1.97 ± 0.09	3.05 ± 0.15	6.87 ± 0.33	5.67 ± 0.30	11.16 ± 0.63	17.04 ± 0.95
$D_P > 50$ nm #/m^3 [10^{14}]	2.19 ± 0.12	2.71 ± 0.10	2.70 ± 0.11	2.54 ± 0.11	2.71 ± 0.11	2.48 ± 0.12	2.25 ± 0.10
D_P = 5.6-560 nm #/m^3 [10^{14}]	5.05 ± 0.21	4.68 ± 0.19	5.75 ± 0.25	9.41 ± 0.44	8.38 ± 0.40	13.64 ± 0.74	19.29 ± 1.06
DGM (nm)	51.04 ± 1.75	51.93 ± 1.93	30.13 ± 2.56	36.95 ± 2.39	21.26 ± 2.37	24.90 ± 2.59	18.28 ± 1.97
75% load							
$D_P < 20$ nm #/m^3 [10^{14}]	0.18 ± 0.01	0.23 ± 0.01	0.26 ± 0.02	0.36 ± 0.02	0.20 ± 0.01	0.41 ± 0.03	0.71 ± 0.05
$D_P < 50$ nm #/m^3 [10^{14}]	2.42 ± 0.09	1.98 ± 0.08	1.94 ± 0.09	1.97 ± 0.08	2.29 ± 0.12	2.35 ± 0.13	9.13 ± 0.51
$D_P > 50$ nm #/m^3 [10^{14}]	8.10 ± 0.33	7.38 ± 0.27	6.70 ± 0.26	6.35 ± 0.28	7.28 ± 0.33	7.44 ± 0.34	7.02 ± 0.35
D_P = 5.6-560 nm #/m^3 [10^{14}]	10.52 ± 0.43	9.36 ± 0.35	8.64 ± 0.56	8.32 ± 0.37	9.57 ± 0.45	9.79 ± 0.47	16.15 ± 0.86
DGM (nm)	67.50 ± 1.61	66.53 ± 1.67	71.44 ± 1.60	66.45 ± 1.66	70.28 ± 1.78	70.37 ± 1.71	32.70 ± 2.65

Table S3 List of the gens up- and down-regulated in A549 cells after 6 h exposure to particles derived from both FBCs-doped and undoped ULSD fuels

	ULSD vs Control		Ce100 vs Control		Fe100 vs Control		Ce100 vs ULSD	Fe100 vs ULSD
Group	Up-regulated	Down-regulated	Up-regulated	Down-regulated	Up-regulated	Down-regulated	Up-regulated	Up-regulated
Transcription	FGF2 FST HNF1B NR5A2 PPARG SOX8 TCEAL1 TGFB1I1	CEBPA DDIT3 EGR1 EGR2 FOS FOSB HOXA5 KLF10 NR4A2 RASD1 TOB1 TRAPPC2P1 TRIB3		DDIT3 FOS KHDRBS3 MNT NR4A2 NR1D2 SP4 TOB1 TRAPPC2P1 TRIB3 ZNF329	NR5A2 PPARG PPARGC1A			DDIT3 EGR1 EGR2 FOS
Cell proliferation /growth/cycle /aging	FGF2 FGFBP1 IRS1 NR5A2 PLA2G4A PPARG RERG TGFB1I1 TNS3 VIPR1		CD38 CDC7 CRIP2 FGFBP1 IRS1 LRP5 MUC5AC PLA2G4A PPARG PRAME RARRES1 RERG TGFB1I1 TNS3 VIPR1	ASNS CDKN2D CTGF CYR61 DDIT3 FOS GADD45B MNT OSGIN1 UHMK1	ARID5B ENO3 FGFBP1 IFITM1 IGFBP1 IL7R IRS1 NR5A2 PLA2G4A PPARG RERG TGFB1I1 VIPR1	CYR61 CTGF OSGIN1		DDIT3 FOS
Metabolism	ABCA1 ADORA2B ALDH1A3 BAAT FGF2 HNF1B HRH1 IRS1 NR5A2 PLA2G4A PPARG TGFB1I1 SOX8	CBS CEBPA DDIT3 EGR1 EGR2 EIF4EBP2 FOS FOSB HOXA5 KLF10 NR4A2 PHGDH RASD1 TRAPPC2P1 ZFP36	ALDH1A3 BAAT C9ORF3 CYP1A1 CYP3A5 DHRS9 FA2H HMGCS1 HNF1B IRS1 NR5A2 PLA2G4A PPARG SERPINA3 SLC19A3 TNFRSF1A	CBS CDKN2D TRIB3 GADD45BV VLDLR	ABCA1 ACOX2 ADORA2B BAAT C9ORF3 CYP1A1 DHRS9 FA2H IRS1 NR5A2 PLA2G4A PPARG PPARGC1A SOX8 TGFB1I1 VAV3	ASNS CBS FAM129A GPT2 RIB3 PHGDH VLDLR		DDIT3 EGR1 EGR2 FOS
Stimulus	ACTA1 ADORA2B IGFBP1 IL7R IRS1 PLA2G4A	ASNS CYR61 DDIT3 DUSP1 EGR1 EGR2	ADORA2B CD38 HMGCS1 IGFBP1 IRS1 RERG	ASNS CDKN2D CYR61 DDIT3 FOS IRS2	ADORA2B CYP1A1 FOXA3 IGFBP1 IRS1 PLA2G4A	ASNS EIF4EBP2 TFF1 VLDLR		

	PPARG RERG	EIF4EBP2 FOS KLF10 NR4A2 VLDLR	PLA2G4A PPARG TFF1 TNFRSF1A	NR4A2 VLDLR	PPARG PPARGC1A			
Cell adhesion	FAIM3 NEXN TGFB1I1 TNS3	CTGF CYR61		CTGF CYR61		CTGF CYR61		
Signal transduction	ABCA1 ARL4C BCAR3 DKK1 FGF2 IRS1 RERG RGS2 TGFB1I1	CTGF, DDIT3 DUSP1, DUSP5, EIF4EBP2, FOS, KLF10, TOB1	DKK1 IRS1 PRAME RGS19 TGFB1I1		ABCA1 ADORA2B ARID5B ARL4C DKK1 FST IFITM1 IGFBP1 IL7R IRS1 PPARGC1A RERG RHOU RGS17 RGS19 TGFB1I1 VAV3 VIPR1 WNT5A			
Response to organic substance /inorganic substance /drug	ACTA1 ALDH1A3 BCAR3 HNF1B IGFBP1 IRS1 PLA2G4A PLIN2 PPARG RERG	ASNS CYR61 DDIT3 DUSP1 EGR1 EGR2 EIF4EBP2 FOS KLF10 NR4A2 VLDLR	ALDH1A3 CD38 CYP1A1 ENO3 HMGCS1 HNF1B IGFBP1 IRS1 PLA2G4A PLIN2 PPARG, RERG, SERPINH1 TFF1 TNFRSF1A		ALDH1A3 CYP1A1 ENO3 PLIN2 PPARG	ASNS CYR61 EIF4EBP2 TFF1 VLDLR		
Response to reactive oxygen species		DDIT3 DUSP1 DUSP5 FOS SRXN1			ACOX2 ALDH1A3 CYP1A1 DHRS9 HMOX2 FA2H PPARGC1A			FOS DDIT3
Regulation of inflammatory response	ADORA2B PLA2G4A PPARG	DUSP1 DUSP5	ADORA2B GPX2 PLA2G4A PPARG TNFRSF1A		ADORA2B PLA2G4A PPARG		CFB SERPINA3	
Transport	ABCA1 ADORA2B	SLC1A4 SLC1A5	ADORA2B CD38		ABCA1 KCNN4	SLC1A4 SLC1A5		

FGF2	IRS1	PLIN2
IRS1	INHBB	PPARG
KCNN4	KCNN4	SLC16A6
PLA2G4A	PLA2G4A	
PLIN2	PLIN2	
PPARG	PPARG	
NR5A2	SLC16A6	
SLC16A6		

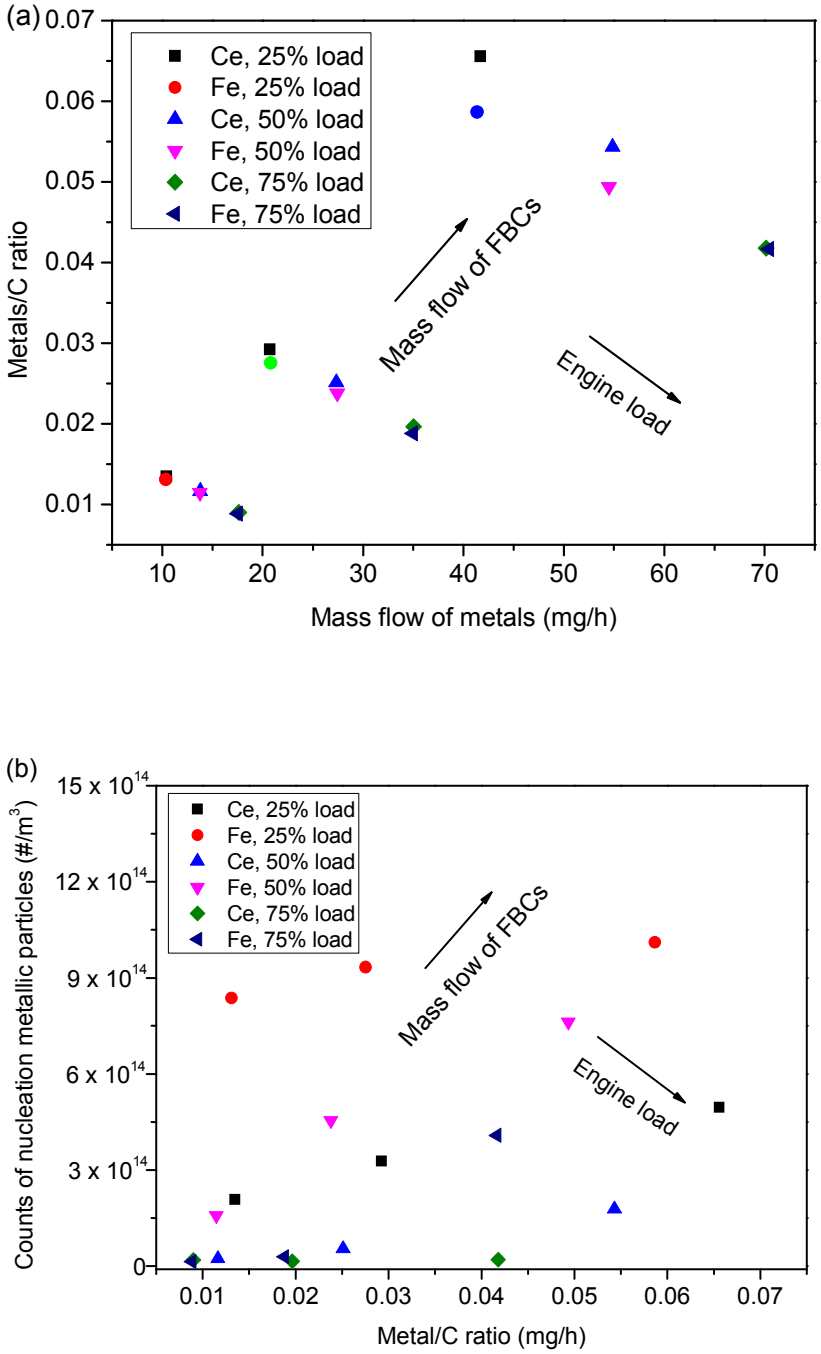

Figure S2 The relationship (a) between mass flow of metals and metal/C ratios, and (b) between metal/C ratios and the counts of metallic nanoparticles

References

(1) Sajith, V.; Sobhan, C.; Peterson, G. P.; Experimental investigations on the effects of cerium oxide nanoparticle fuel additives on biodiesel. Adv. Mech. Eng. **2010**, *2*, 1-6.

(2) Miller, A.; Ahlstrand, G.; Kittelson, D.; Zachariah, M. The fate of metal (Fe) during diesel combustion: morphology, chemistry, and formation pathways of nanoparticles. Combust. Flame **2007**, *149*, 129-143.

(3) Nash, D. G.; Swanson, N. B.; Preston, W. T.; Yelverton, T. L. B.; Roberts, W. L.; Wendt, J. O. L.; Linak, W. P. Environmental implications of iron fuel borne catalysts and their effects on diesel particulate formation and composition. J. Aerosol. Sci. **2013**, *58*, 50-61.

(4) Lu, T.; Cheung, C. S.; Huang, Z. Influence of waste cooking oil biodiesel on the particulate emissions and particle volatility of a DI diesel engine. Aerosol Air Qual. Res. **2013**, *13*, 243-254.

(5) Stratakis, G. A.; Stamatelos, A. M. Thermogravimetric analysis of soot emitted by a modern diesel engine run on catalyst-doped fuel. Combust. Flame **2003**, *132*, 157−169.

(6) Jalava, P.; Salonen, R. O.; Halinen, A. I.; Sillanpaa, M.; Sandell, E.; Hirvonen, M. R. Effects of sample preparation on chemistry, cytotoxicity, and inflammatory responses induced by air particulate matter. Inhal. Toxicol. **2005**, *17(2)*, 107-117.

(7) Koike, E.; Hirano, S.; Furuyama, A.; Kobayashi, T. cDNA microarray analysis of rat alveolar epithelial cells following exposure to organic extract of diesel exhaust particles. Toxicol. Appl. Pharmacol. **2004**, *201*, 178-185.

(8) Ho, S. S. H.; Yu, J. Z. In-injection port thermal desorption and subsequent gas chromatography-mass spectrometric analysis of polycyclic aromatic hydrocarbons and n-alkanes in atmospheric aerosol samples. J. Chromatogr. A **2004**, *1059*, 121−129.

(9) Heywood, J. B. Internal combustion engine fundamentals. McGraw-Hill, New York, 1988.

(10) Lee, D.; Miller, A.; Kittelson, D.; Zachariah, M. Characterization of metal-bearing diesel nanoparticles using single-particle mass spectrometry. J. Aerosol. Sci. **2006**, *37(1)*, 88-110.

(11) Schneider, J.; Hock, N.; Weimer, S.; Borrmann, S. Nucleation particles in diesel exhaust: Composition inferred from in situ mass spectrometric analysis. Environ. Sci. Technol. **2005**, *39*, 6153-6161.

(12) Zhang, J.; Megaridis, C. M. Soot suppression by ferrocene in laminar ethylene/air nonpremixed flames. Combust. Flame **1996**, *105(4)*, 528-540.

(13) Bladt, H.; Schmid, J.; Kireeva, E. D.; Popovicheva, O. B.; Perseantseva, N. M.; Timofeev, M. A.; Heister, K.; Uihlein, J.; Ivleva, N. P.; Niessner, R. Impact of Fe content in laboratory-produced soot aerosol on its composition, structure, and thermo-chemical properties. Aerosol Sci. Technol. **2012**, *46*, 1337-1348.

(14) Song, J.; Wang, J.; Boehman, A. L. The role of fuel-borne catalyst in diesel particulate oxidation behavior. Combust. Flame **2006**, *146*, 73-84.

(15) Jung, H.; Kittelson, D. B.; Zachariah, M. R. The influence of a cerium additive on ultrafine diesel particle emissions and kinetics of oxidation. Combust. Flame **2005**, *142 (3)*, 276-288.